Automatic Estimation of Oil Seep Locations in Synthetic Aperture Radar Images

4 authors:

Gopika Suresh
Nanyang Technological University
22 PUBLICATIONS **89** CITATIONS

Christian Melsheimer
Universität Bremen
66 PUBLICATIONS **1,051** CITATIONS

Jan-Hendrik Körber
Universität Bremen
8 PUBLICATIONS **414** CITATIONS

Gerhard Bohrmann
Universität Bremen
874 PUBLICATIONS **10,082** CITATIONS

Some of the authors of this publication are also working on these related projects:

Project   SAR for land cover clasification View project

Project   Sea Ice project of ESAs Climate Change Initiative (SICCI) View project

Automatic Estimation of Oil Seep Locations in Synthetic Aperture Radar Images

Gopika Suresh, *Graduate Student Member, IEEE*, Christian Melsheimer, Jan-Hendrik Körber, and Gerhard Bohrmann

Abstract—A framework for the automatic detection of natural oil slicks and estimation of their associated oil seeps using synthetic aperture radar (SAR) images is presented, and the methodology used has been explained in detail. The designed detection system is the first automatic oil seep estimation system known to exist. The system detects oil slicks in individual SAR images and estimates their origins on the sea surface. Spatial clustering of temporally recurrent slick origins is conducted in order to estimate the locations of the associated oil seeps on the sea floor. The system is implemented in the programming language Python and a direct rule-based approach is employed for the classification unit. A data set of 178 images of the Black Sea acquired by ENVISAT's Advanced Synthetic Aperture Radar was used to test the algorithm. In this paper, the methodology used to design the algorithm and the automatically estimated oil seep locations are reported. The efficiency of the system with respect to manual detection is discussed.

Index Terms—Advanced Synthetic Aperture Radar (ASAR), Automatic detection, classification, ENVISAT, feature extraction, oil seep, oil slick, synthetic aperture radar (SAR).

I. Introduction

NOT all of the crude oil in the ocean is released from anthropogenic sources. In 2003, the National Academy of Sciences published that about 47% of the crude oil input into global oceans were from natural oil seeps [1]. The Woods Hole Oceanographic Institution states that "as much as one half of the oil that enters the coastal environment comes from natural seeps of oil and natural gas" [2]. These seeps, abundant in the Gulf of Mexico and in other coastal margins worldwide [3], are leaks of liquid and gaseous hydrocarbons fed by subsurface deposits of oil and gas [4]. Faults or fractures in the seabed provide natural fluid pathways through which gas bubbles, sometimes coated with oil, are released into the water column. While most of the bubbles dissolve in the water column, a certain amount reaches the surface where the gas will be released into the atmosphere and the oil forms an oil slick on the sea surface [4].

Oil seeps provide sites where the evolution and ecology of crude oil in the marine environment can be studied [5]. Since oil seeps often entrain gas, particularly methane, locating them could provide an indication of the location of natural sources of these greenhouse gases [4].

The locations of many active oil seeps have been discovered by hydroacoustics and other field sampling techniques [3]. However, these techniques are expensive and time consuming. Satellites equipped with synthetic aperture radar (SAR) are the most efficient and superior sensors for oil spill detection [6] and provides a well-established alternative. This is mainly due to their global coverage in high horizontal resolution, independence of weather and daylight conditions, and the wide availability of data [6].

Oil slick detection in SAR images is possible because of the dampening effect that oil has on the short gravity–capillary waves present on the ocean surface [7]. These waves have wavelengths in the centimeter to decimeter range, producing radar backscatter according to Bragg scattering theory and are hence, also called Bragg waves [7]. Due to the dampening effect, oil slicks appear dark against the brighter radar backscatter produced by Bragg waves. A precondition for detecting these slicks on the sea surface is that the wind is strong enough to generate Bragg waves (2–3 ms^{-1}) [7] and the ideal wind conditions for oil slick detection was found to be between 3 and 7 ms^{-1}[8]. If the wind speeds are too low, the contrast between slicks and their surroundings are too low for detection and at higher wind speeds, the slicks tend to break up, hindering detection. Weathering processes such as evaporation, emulsification and dispersion [6] also affect the visibility of oil slicks.

Automatic detection and identification of natural oil slicks in SAR images is a very complex task because of the presence of look-alikes (L-As). These occur in areas where low wind conditions produce extensively dark areas, from man-made oil spills or biogenic films. The discrimination between natural oil slicks and L-As is challenging, even for a human operator, which emphasizes the need for automatic detection. We aimed to develop an automatic system that detects dark objects and distinguishes between natural oil slicks and L-As and estimates the locations of oil seeps on the sea floor. This would reduce or even omit the workload on human operators who have to manually detect the same, particularly with the increased amount of SAR data available [6]. The advantage of using an automatic algorithm is not just the reduction in processing time, but also the global coverage that can be accomplished. The presented algorithm has been implemented in the programming language Python and uses a novel technique for discrimination between

slicks and L-As. Though many automatic oil spill detection algorithms exists, no completely automatic oil slick and oil seep estimation algorithms have been reported. The algorithm runs completely automatic once the user specifies the mode of operation and the clustering distance for seep estimation (both are explained in Section 5).

II. STATE OF THE ART

There have been many studies aimed at oil spill detection using SAR images but no completely automatic natural oil seep estimator exists. A review of some of the automatic detection algorithms used for oil spill detection is presented in [6]. Some previously used segmentation, or dark spot extraction techniques, are adaptive thresholding [9], hysteresis thresholding [10], edge detection using Laplace of Gaussians or Difference of Gaussians [11], wavelets [12] and mathematical morphology [13]. Neural network-based segmentation were demonstrated in [3], [14], and [15]. In semiautomatic oil spill detection, experienced human interpreters classify the segmented dark objects as slicks or L-As. Automatic algorithms employ classifiers to do the same. Feature-based classifiers use features based on geometry, shape, and physical characteristics of the backscatter of the segmented dark object or contextual features describing the slick in relation to its surrounding [16] to classify objects. Classifiers using a Gaussian density function-based statistical model approach [9], a Mahalanobis classifier [17] and neural networks have also been successfully used in [3] and [15], [18], to classify oil spills from L-As. Previous studies have used the Unsupervised Semivariogram Textural Classifer [19]–[22] for slick detection and classification of slicks from L-As. Manual oil seep location estimation was conducted in [23], and semiautomatic techniques such as a Genetic Algorithm [24] for determining clusters of slicks and their origins, the theory of near inertial oscillation [25] for oil seep trajectories determination and texture-classifying neural network algorithm in [3] have been developed. While many automatic slick detection and semiautomatic seep location algorithms exist, no fully automatic seep location algorithm was reported, apart from the preliminary version [26] of our presented algorithm.

III. TEST SITE

The Black Sea is located between Ukraine, Russia, Georgia, Turkey, Bulgaria, and Romania. It has a maximum depth of approximately 2200 m, a surface area of 420 000 km^2 and represents the largest land-locked basin in the world [27] and surface reservoir of dissolved methane [28]. It is largely anoxic due to the high methane oxidation rates and restricted water mass exchange [28]. A lot of research has been conducted about the sources of methane in the Black Sea, but very little is known about oil seeps. Until now, one site located north-east of the Turkish city of Rize [29] and 11 sites [named Colkheti Seep, Pechori Mound, G1, G2, G2b, G3, G4, G5, G5b, G6, and G6b] offshore Georgia [30] have been discovered (see Fig. 1). It has been suggested that the exclusive occurrence of oil seeps in the Eastern Black Sea is related to the combination of the depth of hydrocarbon deposits, compressional tectonics fostering diapiric sediments and fluid migration, and the relatively
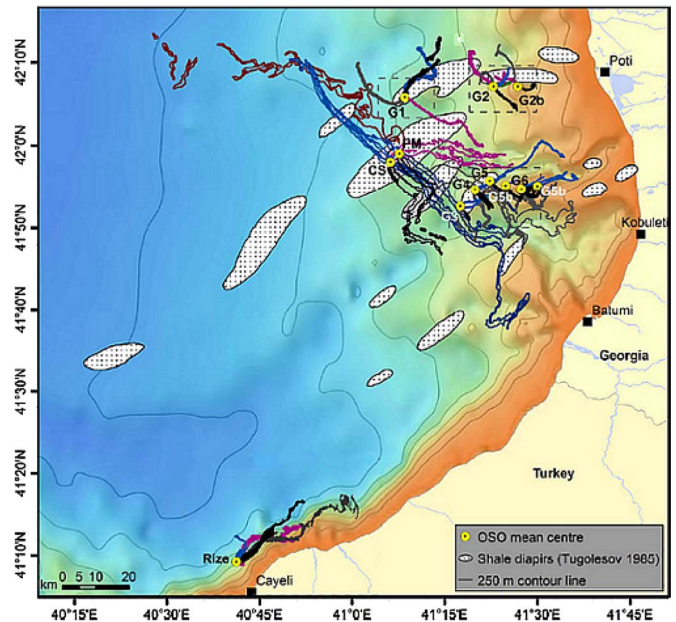

Fig. 1. Illustration of oil slicks identified on ENVISAT ASAR images. Filled polygons are slicks from the recently reported seeps (G1, G2, G2b, G3, G4, G5, G5b, G6, G6b). The slicks from the Pechori Mound (PM) and Colkheti Seep (CS) are shown as empty polygons. Bathymetry: GEBCO 1 min [30].

thin sedimentary overburden on the potential source rocks [30]. Thermal modeling of hydrocarbon generation suggests that, at present, thermocatalytic processes produce gas in the central parts of the Black Sea, whereas oil is generated only at the basin's margins, increasing chances of finding oil emerging from seeps in the margins [29].

IV. DATASET USED

A data set of 178 images from ENVISAT's ASAR sensor was used [see Fig. 2(a)] with a temporal coverage of 9 years from 2002 2011 [see Fig. 2(b)]. Acquired in different imaging modes, 127 of these were in image mode precision (IMP), 52 images in wide swath mode (WSM), and 3 images were in image mode medium (IMM). These modes have scene sizes of 100 km × 100 km for IMP images, 400 km × 400 km and 56 km–100 km in across-track direction for WSM images and up to 4000 km for a stripe in along-track direction in IMM images. Their pixel spacing's are 12.5 m for images acquired in IMP mode and 70 m–75 m for both IMM and WSM modes.

V. ASLE

The SAR signature of an oil slick will depend on the wavelength of small surface Bragg waves, the radar wavelength and the incidence angle of the sensor [3]. The contrast between the oil slick and its surrounding, as well as the shape of the slick, depends on parameters like the wind speed and sea state, ocean currents and the magnitude of oil seepage [3]. A preliminary version of the automatic seep location estimator (ASLE) was reported in [26]. The ASLE system is implemented as two main units: An Automatic Slick Detection Unit (ASDU) that detects oil slicks and estimates their origins in individual SAR images,

Metadata information such date of acquisition, incidence angle, orbit description, calibration factor, and corner coordinates are initially extracted to a separate file. The ASDU is designed to process the data in two modes: MODE-R and MODE-S. MODE-R, with relaxed classification rules, produces fewer misses, but may generate more false detections. MODE-R is designed for small data sets where every missed slick will matter. MODE-S consists of stricter classification rules and should be used with larger data sets. In each mode, the ASDU processes the SAR images in two branches (see Fig. 3): the first branch calculates the Normalized Radar Cross Section (NRCS) values from the SAR image digital numbers as per [31]

$$\sigma^o_{i,j} = 10 * \log \left\{ \frac{DN^2_{i,j}}{K} \sin(\alpha_{i,j}) \right\} \qquad (1)$$

where $DN^2_{i,j}$ is the digital number or pixel intensity for the pixel (i, j), $\alpha_{i,j}$ is the incidence angle for the pixel i, j and K is the absolute calibration constant

Georeferencing and landmasking is then performed on the NRCS value image and the image is saved for further use. The second branch of the ASDU processes the SAR image in seven steps (see Fig. 3). These are: converting digital numbers into gray values, georeferencing and landmasking, speckle filtering, segmentation or dark objects detection, object feature extraction, object classification, and finally, slick origin estimation. In the first step, the original SAR image with digital numbers is converted from 16 to 8 bits and byte scaled using a min–max algorithm that thresholds the image to 99.73% of the gray value distribution as per [32]. Thereafter, land-masking is done using the matplotlib basemap library of Python, which uses a 1.25-min spaced Global Self-consistent, Hierarchical, High-resolution Shoreline database coastline mask [33]. In the third step, speckle filtering of the grayscale image is achieved using a combination of a 3×3 Enhanced Lee filter followed by a 5×5 Enhanced Lee filter used previously in [32]. To maximize the contrast between the potential slicks and water, histogram equalization is performed. The remaining steps of the ASDU are explained in the subsequent sections.

A. Segmentation

Since oil slicks appear dark in SAR images, the first task is to extract these dark regions. A thresholding based on a constant is not preferred because of the variations in backscatter intensities due to sea state and surface roughness (influenced by wind and ocean current) and incidence angle of the satellite. Mean filters are not used as they smooth the edges of dark objects, particularly when a large window size is used [13]. Adaptive thresholds behave well for removing noise and tracking low frequencies. Hence, we use a nonlinear filter implemented using mathematical morphology as in [13] and [34] where the adaptive threshold is calculated using a combination of grayscale closing and opening of the original image using a structuring element (SE) of a set size. Pixels with values above the threshold are set to 1 representing open water, whereas those
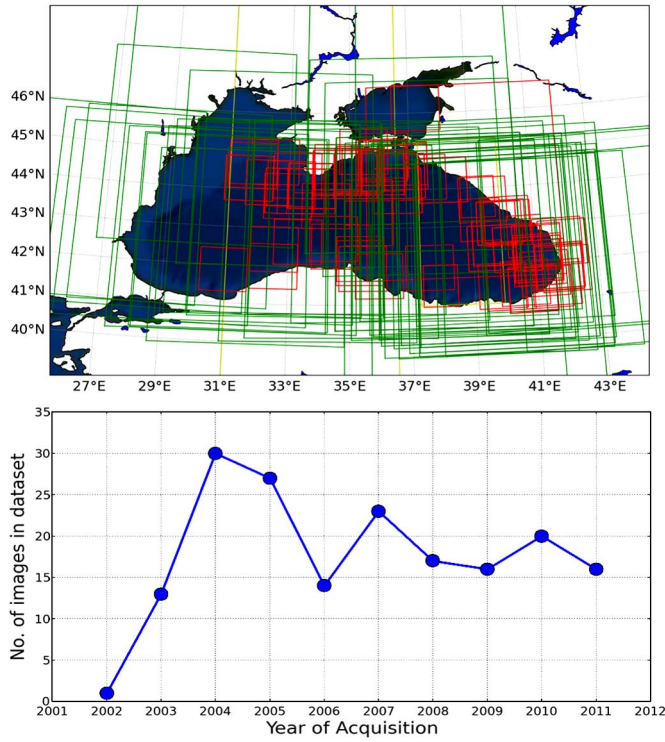

Fig. 2. (a) Spatial Coverage and SAR scene footprints. (Red) IMP images. (Yellow) IMM Images. (Green) WSM images. (b) Temporal coverage of the SAR images.
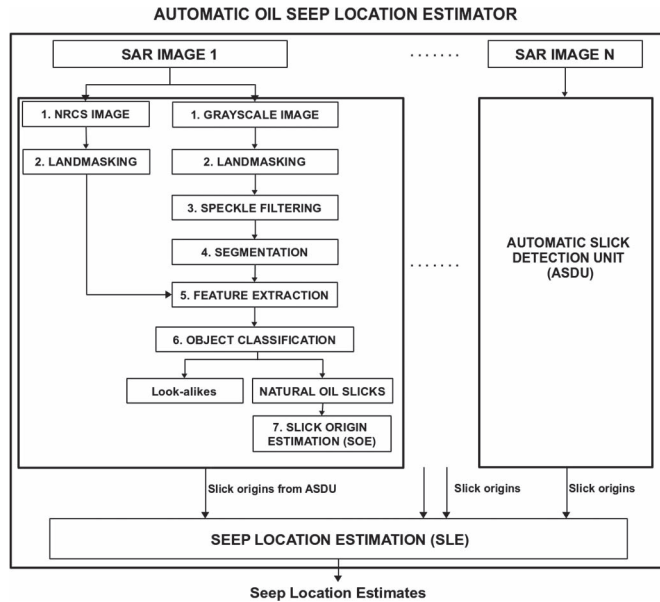

Fig. 3. Designed ASLE using N images.

and a seep location estimator (SLE) that uses the previously estimated slick origins to estimate the geographic location of oil seeps on the sea floor (see Fig. 3). The system is implemented such that oil slicks can be detected in single SAR images, but seep locations can be estimated only when a larger data set of more than 2 images is provided, due to the spatial clustering routine.

in below, are set to 0 representing possible slick pixels. The adaptive threshold $\sigma_{\text{th}}(x, y)$ can be calculated from [13] as

$$\sigma_{\text{th}}(x, y) = \phi_B \left\{ \gamma_B \left[f(x, y) \right] \right\} \tag{2}$$

which is the closing ϕ_B of the opening γ_B of the image $f(x, y)$, and B is the SE. Details about the morphological segmentation techniques are presented in [9].

The size of the SE affects the number of dark pixels being segmented and in turn affects the shape of the slick. If the SE size is too small, too many dark pixels are segmented in open waters but most of the slick pixels are preserved. On the other hand, if the SE size is too large, fewer dark pixels are segmented over open water but some slick pixels are lost. A SE of size 55×55 pixels was chosen to best preserve the entirety and shape of the slick. After thresholding, pixels in an 8 neighborhood are joined to form dark objects. Small objects less than 0.065 km^2 in IMP and less than 0.7 km^2 in WSM and IMM are excluded from further processing.

B. Object Feature Extraction

The following features can be extracted by the feature extraction unit.

1) Geometric features
   a) Spread (S): It has a generally low value for thin and elongated shapes and a higher value for more circular shapes. If $\lambda 1$ and $\lambda 2$ are the eigenvalues derived from the eigenvalue decomposition of the principal component analysis (PCA) vectors of the dark objects, then spread is defined from [18] as

$$S = \frac{100 * \lambda 2}{\lambda 1 + \lambda 2}. \tag{3}$$

   b) Area (A) [km^2]: This is the number of pixels in the dark object multiplied by the pixel spacing of the image.
   c) Aspect Ratio (AR): Ratio of the minor axis and major axis computed from the PCA. It takes low values for linear shapes and high values for irregular shapes.
   d) Width [km]: Minor axis of the PCA. We assume that the width is uniform.
   e) Length [km]: Major axis computed from the PCA.
   f) Perimeter (P) [km]: Pixels constituting the perimeter of the dark object.
   g) Complexity: It is defined from [18] as

$$C = \frac{P}{2\sqrt{\pi A}} \tag{4}$$

   where P is the perimeter, and A is the area
   This feature will take small values for simple geometries and larger values for more complex shapes.
   h) Center of Mass [pixels]: Derived from the eigenvalues of the PCA. This is useful to find the position of and distance between objects.

2) Radiometric Features:
   These features are calculated using the NRCS values of the SAR images and are:

   a) Object Backscatter Mean (OMEAN) [dB]: The mean of the NRCS values of the dark object pixels.
   b) Object Backscatter Standard Deviation (OSD) [dB]: The standard deviation of the NRCS values of the dark object pixels.
   c) Background Backscatter Mean (BMEAN) [dB]: Mean of the NRCS values of the pixels in the enclosing rectangle around the dark object.
   d) Background standard deviation (BSD) [dB]: This is measured by analyzing the variation in NRCS values of the pixels in an enclosing rectangle within a user-defined distance from the object. The distance between the object and the enclosing rectangle is chosen as 10 pixels.
   e) Mean Contrast (MeanC) [dB]: This is the difference between the mean background backscatter and the mean object backscatter.
   f) Max Contrast (MaxC) [dB]: This is the difference between the maximum background backscatter and the minimum object backscatter.
   g) Standard Deviation Ratio (SDR): Defined as the ratio of object standard deviation to BSD.
   h) Mean Ratio (MR): Ratio of object mean backscatter to background mean backscatter (BMEAN).

3) Texture Features:
   a) Object Power to Mean Ratio (OPMR): Defined as OSD/OMEAN of the dark object. According to [16], high PMR values indicate low wind regions and hence high contrast between slick and surroundings is expected due to less weathering of the slick from wind. Vice versa is applicable for low PMR values.
   b) Background PMR (BPMR): Defined as the BSD/ BMEAN of the background around the dark object within the previously defined enclosing rectangle.

C. Object Classification

The classification algorithm must try to resemble the method that the human brain uses to choose between natural oil slicks and L-As. We chose a decision-based classifier that employs an array of classification rules due to its speed and simplicity.

1) Training Dataset: To understand the characteristics of natural oil slicks in comparison to oil spills and other L-As, a training data set was created. This consisted of SAR images, in which oil slicks were manually detected by [30] and the presence of seepage from natural sources was confirmed by hydroacoustics, sampling and visual observations [30]. These are referred to as verified oil slicks (VOSs). Our training data set consisted of 11 ENVISAT images acquired in IMP mode and 6 images acquired in WSM. Some examples of the VOSs from [30] are shown in Figs. 4 and 5. L-As were also analyzed to understand how they can be distinguished from oil slicks. Fig. 6 shows examples of some L-As in C-band RADARSAT images that originate from wind shadowing by coastal topography [35]. Apart from wind-related L-As, a C-band SAR sensor is also affected by dampening of radar waves by rain-volume
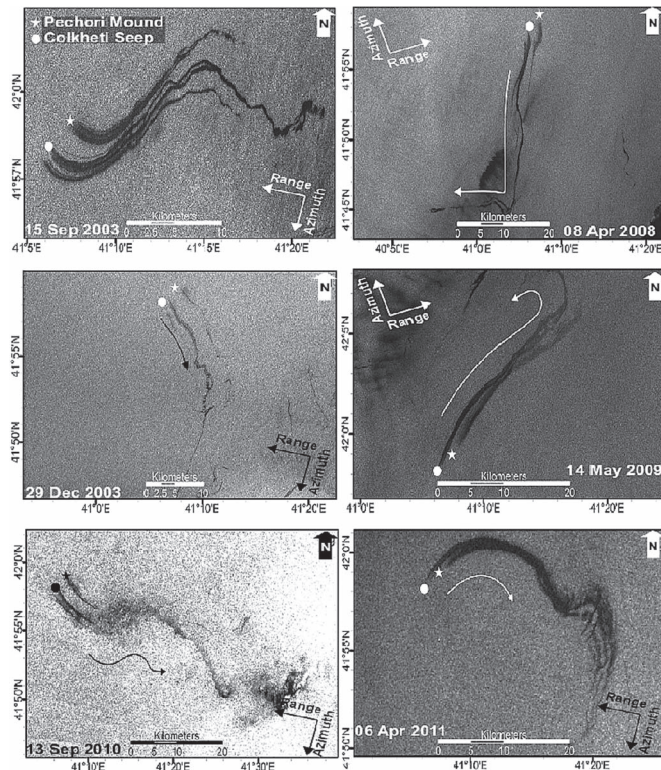
Fig. 4. Subset of ASAR images (modified from [30]) containing VOSs above the Colkheti seep (circle) and Pechori mound (star).
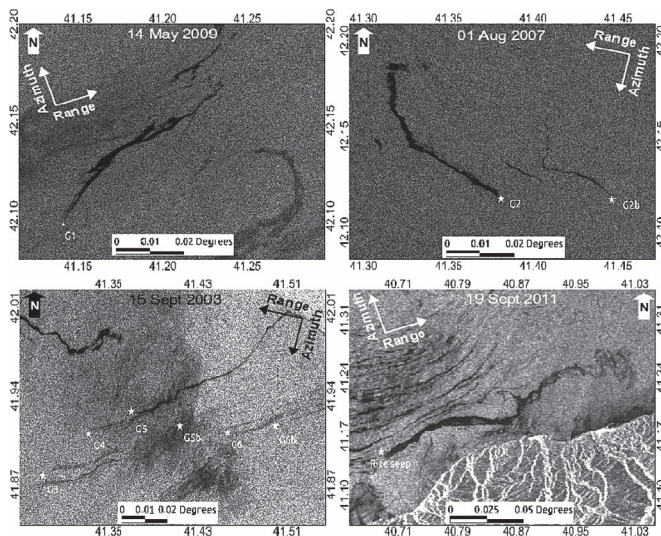

Fig. 5. Subset of ASAR images containing VOSs from seeps identified in [30].

scattering [35] and dampening of Bragg waves by rain-induced turbulence in the upper water layer [36]. L-As could also be attributed to surfactants either from man-made oil spills and natural biogenic slicks produced by plankton.

For a statistical analysis, SAR images in the training data set were landmasked and georeferenced, speckle filtered and segmented as described in Section V-A. Slicks were observed to be segmented in broken segments possibly cause by inhomoge-
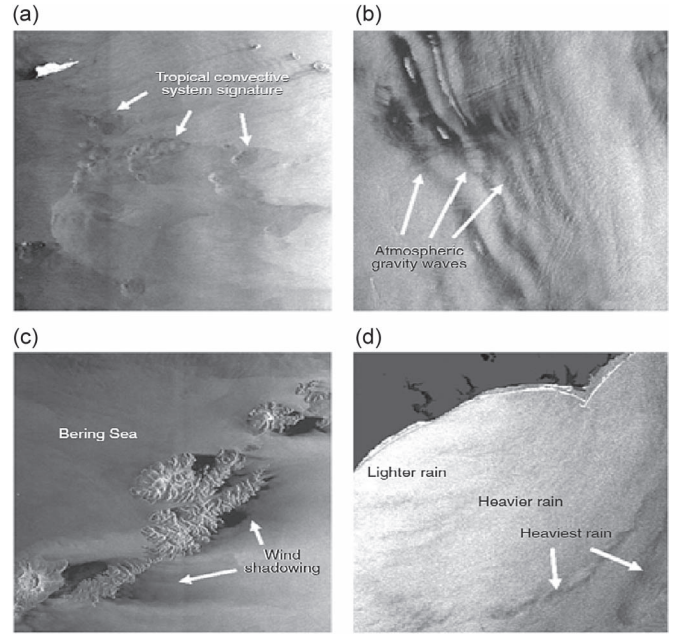

Fig. 6. RADARSAT images showing L-As from (a) tropical convective cells, (b) atmospheric internal gravity wave patterns, (c) shadowing effects produced as wind blows over the islands, and (d) rain cells [35].
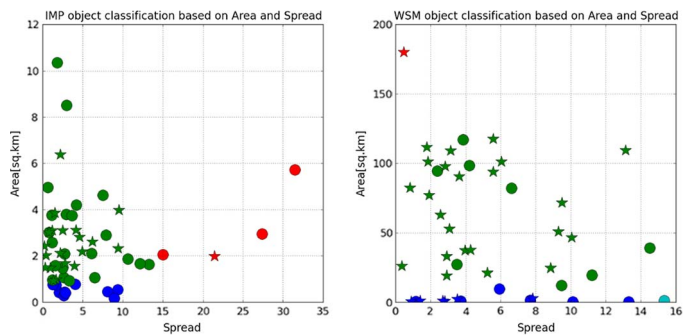
Fig. 7. (Circles) VOS and (stars) L-A object classification based on area and spread features in MODE-R. (Green) Big-long objects. (Blue) Small-long objects. (Cyan) Small-round objects. (Red) Big-round objects.

neous radar backscattering from the slick due to wind and sea-state or due to speckle noise. Since the entire shape of a slick is important for slick origin estimation, a joining procedure was implemented wherein the pixels in dark objects within 0.5 km^2 from each other were joined together. This distance was chosen based on manual analysis of segmented slicks. Features for each dark object were then calculated. Separate analyses were conducted for dark objects in IMP and WSM mode as we observed that these objects had different characteristics and texture in the different ASAR acquisition modes. The two acquisition modes image the ocean SAR features at different scales and must hence be treated separately. We also attribute differences in ocean SAR features in the two modes to the coarser resolution and the sampling employed in level-0 processing of the WSM images. Since the L-A objects chosen for analysis were very similar in appearance to VOSs, discrimination based on only spread and area features was difficult. However, from Fig. 7, we can infer that majority of the VOSs in both IMP and WSM images had low spread values (< 15). Most of the VOSs in the

This article has been accepted for inclusion in a future issue of this journal. Content is final as presented, with the exception of pagination.

6   IEEE TRANSACTIONS ON GEOSCIENCE AND REMOTE SENSING
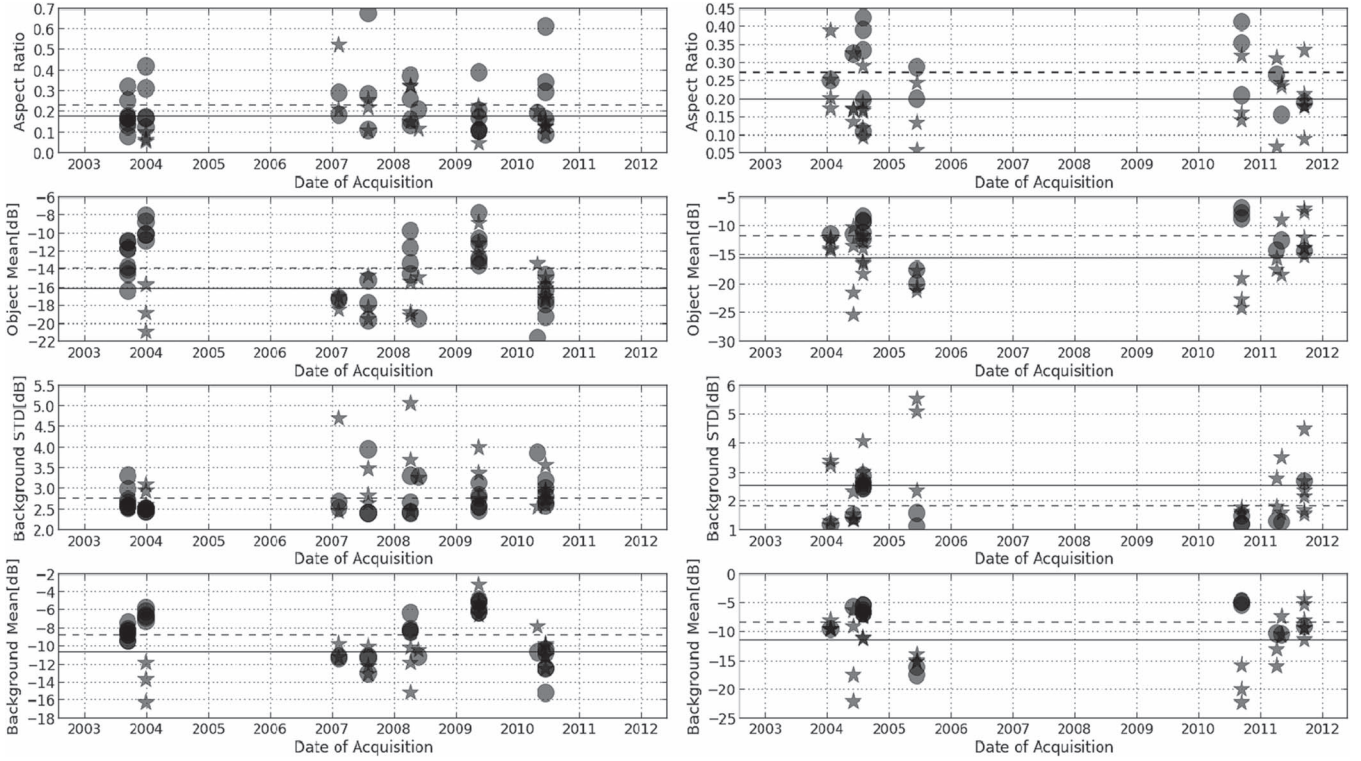

Fig. 8.   (Circles) Plots showing feature values of VOS objects and (stars) L-A. (Dashed line) Mean of the VOS objects. (black line) Mean of the L-A objects. (Left) Features of objects in IMP mode. (Right) Features of objects in WSM mode. (Rows from top to bottom) AR, OMEAN, BSD, and BMEAN.

IMP images in our data set had areas of 5 km^2 or less, and objects in WSM images varied from 10 to 120 km^2 in area. Hence, we chose to exclude objects in WSM images with areas greater than 150 km^2 as they were most likely to be L-As in our training data set. ARs were also found to provide more information about the approximate geometry of the object. VOSs were seen to have AR values ranging from 0.1 to 0.7 with a mean of 0.23 (see Fig. 8).

According to [6], oil dampens the sea surface radar backscatter in the range of 0.6 dB to 13 dB, whereas natural films, in the range of 0.8 dB to 11.3 dB. This shows that it is difficult to distinguish between them based on object mean backscatter alone. From [9], a human operator would have a higher belief that a dark spot is a slick if the surroundings are homogeneous, i.e., BSD is low. Hence, if the BSD is low, the probability of the detected dark object being a slick is higher. This promoted us to analyze the OMEAN, BSD, and BMEAN values for the objects in the training data set.

While the AR is object shape dependent, OMEAN, BMEAN, and BSD are features that are dependent on object backscatter. Most VOSs are seen to have relatively higher OMEAN (-14 to -8 dB), low BSD (less than 3.5 dB) and high BMEAN (-12 to -8 dB) (see Fig. 8). A physical explanation for the relatively higher OMEAN is that oil slicks produce very inhomogeneous backscatter, mainly due to the variation in the amount of oil present in different parts of the slick. Oil slicks have a less weathered and more weathered end depending on the wind speeds and ocean currents. The less weathered end corresponds to the part of the slick formed most recently and

will hence dampen the incidence SAR waves stronger than the more weathered parts of the slick. Slicks also tend to be inhomogeneous because, with time, the lighter compounds in the oil are moved less by wind, whereas the heavier oil is moved more [7].

Low BSD values indicate relatively calmer sea surfaces. Since oil slicks tend to break up at higher wind speeds, objects with low BSD values indicate that sea surfaces are calm enough for the slick to persist for a while. The observed BSDs of the VOSs in the training data set were consistent with this notion. Slicks are dark elongated objects set in a relatively brighter background, i.e., higher values of BMEAN. The physical significance of higher BMEAN values is that if an object is found in a region where the backscatter is very low (very dark region), then these are more likely to be regions of low wind rather than oil slicks Hence, BSD eliminates objects that are situated in very rough sea surfaces, and BMEAN eliminates objects which are found in very dark areas such as low wind areas and rain cells.

2) Object Classification Unit: The rules for object classification were acquired based on our analysis of the training data set. In [26], Area, Spread, OSD, and Mean contrast were used to distinguish between slicks and L-As. Though these features worked well, we chose to use a combination of six features for this present version of the ASLE. IMP and WSM (and IMM) images have different sets of rules due to the different pixel spacings, and because the characteristics of L-As and VOSs were observed to be different in different modes. In addition, different rules have been implemented for MODE-R

This article has been accepted for inclusion in a future issue of this journal. Content is final as presented, with the exception of pagination.

SURESH *et al.*: AUTOMATIC ESTIMATION OF OIL SEEP LOCATIONS IN SAR IMAGES

7

TABLE I
DEFINED OBJECT CLASSIFICATION RULES

Extracted Feature	MODE-R		MODE-S	
	IMP	WSM/IMM	IMP	WSM/IMM
S	$S \leq 15$	$S \leq 15$	$S \leq 14$	$S \leq 12$
A [km^2]	$0.9 < A \leq 150$	$5 < A \leq 150$	$0.9 < A \leq 150$	$5 < A \leq 150$
AR	$0 < AR \leq 0.5$	$0.1 < AR \leq 0.5$	$0.1 < AR \leq 0.5$	$0.15 < AR \leq 0.5$
BSD [dB]	≤ 4	≤ 3	≤ 3.5	≤ 2.5
OMEAN [dB]	> -19	> -20	> -17	> -15
BMEAN [dB]	> -14	> -16	> -17	> -12

and MODE-S. Objects within 0.5 km are first joined to preserve the slick shape. Thereafter, the classification unit has been implemented as follows.

1) Area (A) and Spread (S) values for the dark objects are found in order to determine the basic shape of the object. An object is given the attribute of *long* if its spread value is less than the set threshold, and *round*, if greater. Similarly, an object is *big*, or *small* based on whether its area is greater than or less than the set area threshold, respectively. The objects are hence assigned with attributes of being either *big-long*, *small-long* or *small-round*. The *big-round* objects are immediately disposed based on our statistical analysis of the VOSs in the training data set.

2) A distance criterion is then used to retain *small-long* and *small-round* objects that are within 3 km and 1 km, respectively, from a *big-long* object. This criterion ensures that slicks segmented in broken parts are preserved. The other dark objects are eliminated.

3) ARs are then calculated using PCA. Objects with AR within the rules defined in Table I are retained.

4) BSD, OMEAN, and BMEAN are computed. Objects are retained if their feature values are within the defined rules (see Table I).

D. Slick Origin Estimation

The slick origin is the point on the sea surface where the oil reaches the sea surface. At this point, the oil is the freshest and is expected to have the largest dampening effect on the incident SAR waves. Though this notion has been successfully used to determine slick origins in [30], it did not work accurately when tested with our slick origin detection algorithm. This could be attributed to the presence of speckle noise and loss of slick pixels during the process of filtering and segmentation. Slicks usually tend to be wider at their origin than at the older (trailing) end [4]. However, in some images, it was noticed that the trailing end of the slick was wider than the origin, possibly due to oil accumulation during calm ocean and wind conditions [7]. Our algorithm is hence designed to detect both ends of the slick. The widest end is detected by locating the widest part of the slick using a chessboard distance transformation and thereafter determining the end closest to it. The trailing end is thus located as the end nearest to the thinnest part of the slick segment.

TABLE II
CLASSIFICATION RESULTS OF THE ASDU ON THE TRAINING DATASET

Type of dark Object	No. of dark objects	Objects classified as Oil (%)		Objects classified as L-A (%)	
		MODE-R	MODE-S	MODE-R	MODE-S
VOS (IMP)	35	82.9	65.7	17.1	34.3
VOS (WSM)	15	80.0	40.0	20.0	60.0
L-A (IMP)	21	76.2	33.3	23.8	66.7
L-A (WSM)	30	50.0	23.3	50.0	76.7

E. Seep Location Estimation

The SLE uses the slick origins in the entire data set to estimate the location of the feeding seep on the seafloor. In [4], slick origins within 2500 m from one another are chosen to belong to the same seep cluster. Based on that, our SLE is designed to cluster slick origins within a 2.5-km distance and the mean center of the cluster is estimated as the seep location. During this clustering, both ends of the slick estimated by the slick origin estimation unit are considered. If both ends of the slick are within the same cluster, then the slick end closest to the mean center of the cluster is chosen as the slick origin. The seep location estimates are then plotted on a map. A count of the number of slick origins in each cluster is made. This count describes the number of times a slick was detected in a 2.5-km radius in temporally varying images. A detection percentage, defined as the number of times slicks emerging from the same seep were detected divided by number of SAR images of that area is calculated. The higher the detection percentage, the higher the confidence in the estimated seep location. The end-product of the algorithm is a map of the estimated seep locations and their corresponding detection percentages.

VI. RESULTS

The ASLE is the first of its kind that processes stacks of ocean SAR images to produce seep location estimates automatically. The ASLE was tested first on the training data set and thereafter on the whole data set of 178 SAR images. The seep locations estimated by the ASLE are then compared with known seep sites and seep locations estimated from manual detection [30].

This article has been accepted for inclusion in a future issue of this journal. Content is final as presented, with the exception of pagination.

8   IEEE TRANSACTIONS ON GEOSCIENCE AND REMOTE SENSING
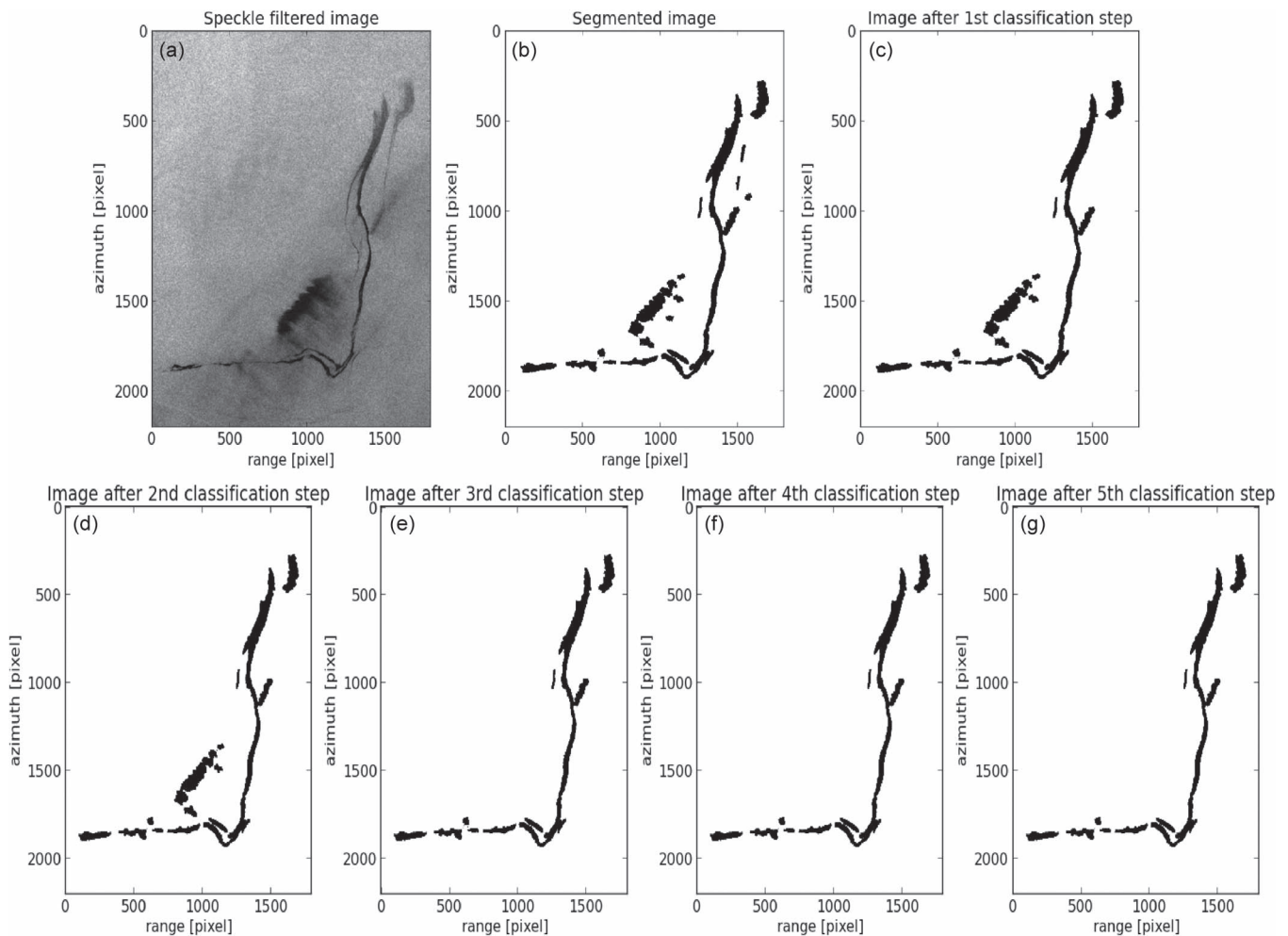

Fig. 9.   Subset of an ASAR IMP image acquired on 08 April 2008. (a) Speckle filtered image. (b) Segmentation results. Classification results in MODE-R based on (c) Area and Spread, (d) AR, (e) OMEAN, (f) BSD, and (g) BMEAN.

A. Results of the ASDU on the Training Dataset

The VOSs and L-As were input to the ASDU separately. The output of the ASDU is shown in Table II and shows the slick detecting efficiency of the ASDU. 82.9% of the input IMP VOSs and 80% in WSM VOSs were classified correctly in MODE-R. When the L-As were considered in MODE-R, 23.8% were correctly classified in IMP images and 50% in WSM images. Correct classification of L-As increases to 66.7% and 76.7% in IMP and WSM images, respectively, in MODE-S, but more VOSs missed, decreasing the classification efficiencies to 65.7% and 40% in IMP and WSM images, respectively.

B. Results of the ASLE on the Entire Dataset

The ASDU, in both modes, processed an image in under 2 h on an AMD Phenom II X4 quad core (3.4 GHz) processor. Dark objects were segmented and their geometric, radiometric and textural features extracted. Objects classified as slicks were retained and their origins determined. Fig. 9 shows the subset of an image acquired on 08 April 2008 at

various stages in the ASDU processing. The final results of the algorithm, a map of the test site with the estimated seep candidate locations and their detection percentages is shown in Fig. 10.

In MODE-R, 1497 seep candidates were estimated by the ASLE algorithm when a spatial clustering of 2.5 km was used. 1306 of the estimated seep candidates were estimated with detection percentages of less than 10%, 191 candidates with detection percentages between 10% and 15% and 14 seep candidates with detection percentages greater than 15%. Fig. 10 shows their location. The yellow dots represent the location of the seep candidates that have detection percentages below 10% and red dots represent seep candidates estimated with detection percentages from 10% to 15%. Green dots are those seep candidates that were estimated with detection percentages greater than 15%. The size of the dot varies according to the count of slick origins in the cluster. The pink triangles represent the sites of the 12 previously known oil seeps from [30]. Nine out of the 12 known seeps locations were estimated in MODE-R. Their corresponding detection percentages are shown in Table III. For MODE S, 426 seep candidate locations were estimated, 396 seep candidates with detection percentages

This article has been accepted for inclusion in a future issue of this journal. Content is final as presented, with the exception of pagination.

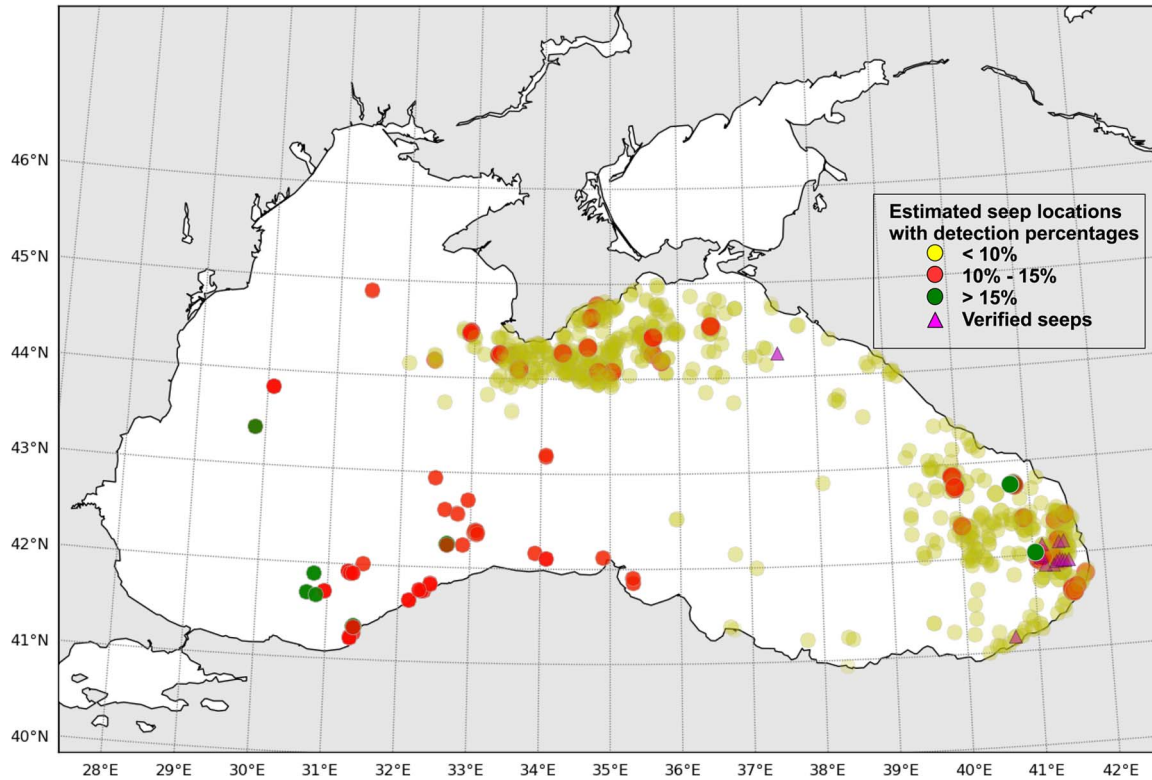SURESH *et al.*: AUTOMATIC ESTIMATION OF OIL SEEP LOCATIONS IN SAR IMAGES

9

Fig. 10. Estimated seep candidate locations in the Black Sea in MODE-R. The size of the dot varies according to the number of origins in a spatial cluster of 2.5 km. The dots represent mean centers of the clusters.

less than 10%, 28 seep candidates with detection percentages between 10% and 15% and 2 greater than 15%. Seven of the known seeps locations were estimated by the ASLE in MODE-S. The detection percentages of the seeps located near the known seeps are shown in Table III.

C. ASLE Versus Human Classification

Efficiency of the ASLE results can be analyzed by comparing the automatic slick detection results to manual detection results. For each of the 12 known seeps, the details used to estimate the seep locations were acquired from [30]. The SAR images with faintly visible slicks, low wind speeds, and L-As around potential slicks were excluded from comparison, mainly because segmentation yields false positives. The remaining SAR images were viewed in a GIS [37] along with their corresponding ASDU outputs. Outlines were created for the slicks that were both automatically and manually detected by [30]. The number of times the ASDU detected a manually detected slick provides us with the slick detection efficiency. The results are shown in Table IV, and a brief description of our results are provided in the following.

At the Colkheti Seep and Pechori Mound, slicks were manually detected in 26 images [38] and are shown in Fig. 11. Three of the 26 images were not present in our data set. Slicks in the images acquired on 28 March 2005, 20 November 2007, 20 November 2008, 11 January 2010, 24 May 2010, and 05 September 2011 were very faint and not segmented by our segmentation unit. The slicks in these images appeared

so similar to L-As that even manual detection was difficult. In the remaining 17 ASAR images, the ASDU detected 13 slicks above the Colkheti Seep and 12 slicks above the Pechori Mound, corresponding to detection efficiencies of 76.4% and 70.5%, respectively (see Fig. 11). Since the two seeps are spatially very close, slicks emerging from them were sometimes segmented as one large slick. The filled polygon shows the three additional slicks that our ASDU has detected.

Similarly, the slicks emerging from the other 11 seeps were analyzed. For site G1, visual inspection of the 19 SAR images, in which slicks were manually detected, showed that only ten images could be considered in our automatic analyses (the other images were either too dark/not in the data set/slicks were too faint to be detected). Four out of these ten slicks were automatically detected by the ASLE on 14 May 2009, 31 July 2006, 02 June 2004, and 15 September 2003 producing a detection efficiency of 40%. For site G2, 4 slicks (29 July 2004, 01 August 2007, 22 March 2010, and 16 June 2010) of the 10 manually detected slicks were automatically detected, producing a detection efficiency of 40%. Three slicks (16 June 2010, 31 July 2006, and 29 July 2004) of the 5 manually detected slicks, were automatically detected for site G2b, producing a detection efficiency of 60%. For the site G3, 1 slick was automatically detected in the image acquired on 15 September 2003 compared with 3 manually detected slicks. However, two more slicks were automatically detected in images acquired on 08 April 2008 and 22 October 2011. For the site G4, 5 slicks were manually detected, and 3 of these (01 August 2007, 13 September 2010, and 15 September 2003) were

TABLE III
DETECTION PERCENTAGES OF THE SEEP LOCATIONS ESTIMATED NEAR THE KNOWN SEEP SITES

Seep Name	Latitude, Longitude [Decimal Degrees]	Detection percentages of estimated seeps (MODE-R, 2.5 km spatial clusters)	Detection percentages of estimated seeps (MODE-S, 2.5 km spatial clusters)	Detection percentages of estimated seeps (MODE-R, 3.5 km spatial clusters)	Detection percentages of estimated seeps (MODE-S, 3.5 km spatial clusters)
G1	42.0959N, 41.1418E	6.67%	-	6.67%	-
G2	42.1176N, 41.3812E	12.2%	7.89%	14.6%	10.5%
G2b	42.1172N, 41.4467E	-	-	4.88%	5.26%
G3	41.8772N, 41.2919E	6.97%	7.50%	6.98%	10%
G4	41.9103N, 41.3318E	6.98%	5.0%	9.30%	7.5%
G5	41.9282N, 41.3713E	11.9%	10.3%	14.3%	12.8%
G5b	41.9184N, 41.4143E	-	-	9.52%	7.69%
G6	41.9113N, 41.4564E	4.76%	5.13%	7.14%	7.69%
G6b	41.9170N, 41.5002E	-	-	4.76%	5.13%
Rize	41.1526N, 40.6874E	8.57%	-	8.57%	-
Colkheti Seep	41.9670N, 41.1042E	17.4%	18.6%	23.9%	20.9%
Pechori Mound	41.9826N, 41.1254E	14.9%	13.6%	19.1%	18.2%

TABLE IV
ASLE DETECTION EFFICIENCIES COMPARED WITH MANUAL OIL SLICK DETECTION

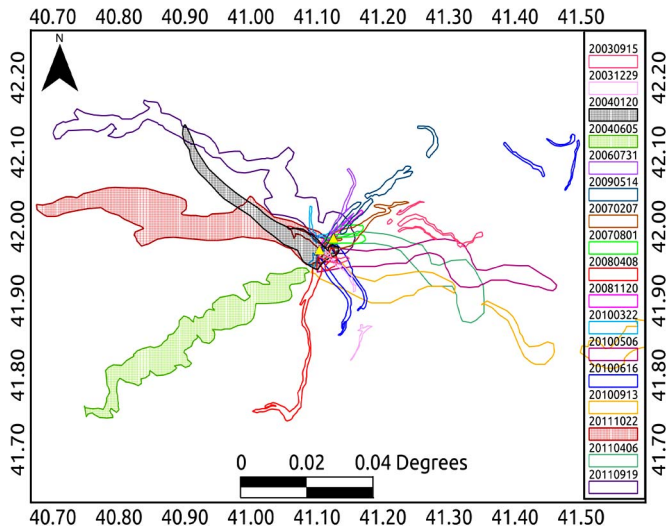| Seep name	Number of images in which slicks were detected as per [30]	Number of images available for automatic slick detection	Number of correctly detected slicks	DETECTION EFFICIENCY
G1	19	10	4	40%
G2	16	10	4	40%
G2b	12	5	3	60%
G3	7	3	1	33%
G4	6	3	1	33%
G5	14	4	3	75%
G5b	14	4	3	75%
G6	9	4	1	25%
G6b	9	4	1	25%
Rize	17	8	5	62.5%
Colkheti Seep	26	17	13	76.5%
Pechori Mound	26	17	12	70.6%

Fig. 11. Outlines of the slicks detected by the ASDU above the Colkheti Seep and Pechori Mound. The filled polygons show the new slicks that were detected by the ASDU, whereas the empty polygons show the slicks reported in [24]. The legend reports the date of acquisition of the SAR images in a YYYYMMDD format.

detected by our algorithm, producing a detection efficiency of 60%. The detection efficiency of the ASDU for slicks above site G5 is higher (80%) as 4 out of the 5 manually detected slicks were automatically detected by the algorithm (01 August 2007, 29 July 2004, 15 September 2003, and 06 April 2011). Apart from the previously detected slicks, an additional slick was detected in the image acquired on 05 November 2003 over the site G5. Slicks above site G6 were manually detected in 4 images, but only one of these slicks was automatically detected (22 March 2010). However, a slick above G6 was automatically detected in the image acquired on 01 August 2007. Five slicks above the Rize seep were automatically detected compared with 8 manual detections, yielding a detection percentage of 62.5%. The ASLE detection efficiencies compared with manual detection is summarized in Table IV.

VII. DISCUSSION

The ASLE produces locations of seep candidates in a completely novel automated process without the aid of a human operator. The results previously presented demonstrate its

This article has been accepted for inclusion in a future issue of this journal. Content is final as presented, with the exception of pagination.

SURESH *et al.*: AUTOMATIC ESTIMATION OF OIL SEEP LOCATIONS IN SAR IMAGES　　11

potential for automatically detecting natural oil slicks and oil seeps from SAR images. Dark spot detection or segmentation is considered a critical step in oil slick detection and the accuracies of feature extraction and classification greatly depend on the accuracy of segmentation [15]. The ASLE segmentation routine, consisting of dark-spot detection and small-area removal, takes 5 s on a 3.4-GHz processor to segment dark objects in a 8192×8836 pixel IMP image. As per [15], the segmentation times for the PCNN model is 7 s on a 512×512 pixel image (2.2-GHz processor) and 11 s in [39]. The larger slicks were noticed to be very accurately segmented, whereas the smaller slicks in the vicinity of large slicks were omitted, particularly in IMP images. While during manual image analyses, contrast enhancement was possible when the image was too dark or too bright, this is not possible during automation. Though the ASDU employs histogram equalization, the contrast between slicks and their surrounding is, in some cases, insufficient for segmentation, prohibiting slick detection.

The results of the ASLE are seep locations estimated with their detection percentages. Please note that all images in the data set were considered in this analysis, irrespective of wind speeds and visibility of slicks, i.e., the images, in which the slick is very faintly visible and/or where the slick is merged with L-As, resulting in the reduction of detection percentages. This will be eliminated in the future by considering wind information and hence eliminating those images with low or high wind. The ASDU was successful in correctly detecting slicks with classification efficiency of 82.9% in comparison to the 78.4% efficiency of the oil spill detection algorithm described in [16] when tested on the training data set. This shows that the defined rules worked efficiently in discriminating oil slicks and L-As. This is demonstrated in Fig. 9(a), where two slicks are visible: the left, longer slick, emerging from the Colkheti Seep and the right, smaller slick, emerging from the Pechori Mound. The dark area close to the center of the Colkheti Seep slick is most likely caused by a rain cell in that region. The dark area due to the rain cell was segmented and was present until the third classification step [see Fig. 9(e)]. The classification based on object mean backscatter effectively removes this L-A. Fig. 9 also shows that the implemented joining procedure has been successful in maintaining the shape and length of the slick even though the slick was segmented as different segments. The effectiveness of the distance criteria used in the object classification unit which helps prevent the loss of smaller slick segments is also demonstrated in Fig. 9.

We also analyzed the results of the ASLE when the spatial clustering distance was increased to 3.5 km. This is mainly because some parts of slicks were not segmented and hence slick origins estimated from these parts would lie a distance away from the visual slick origin. When spatial clustering was increased to 3.5 km, the detection percentages of the seep candidates were seen to increase. In MODE-R, all of the known seep locations were estimated by the ASLE with detection percentages as shown in Table III, and a total of 2261 seep candidate locations were estimated, 54 of which were calculated with detection percentages of 15% and greater. In MODE-S, the number of estimated seep candidates increased

to 684 when a spatial clustering of 3.5 km was used, 9 of which possessed detection percentages of greater than 15%.

Spatial clustering of 3.5 km in depths of 800–1500 m (where the known seeps are located) and considering seeps locations that have been estimated with detection percentages of 15% or greater are optimization techniques for the future seep location estimation. Other ways to improve the ASLE would be to reduce the processing time of the algorithm by optimizing the joining close-segments routine. This routine is important for preserving slick shapes but presently takes 30 min to join close segments in an IMP image and almost 1 h for a WSM image. By reducing the time involved here, the processing time of the ASLE can be brought down to 20–30 min per image. Further improvements to the ASLE would be to incorporate wind-information in order to eliminate images, in which wind-speeds are either too high or too low.

VIII. CONCLUSION

SAR images provide weather and daylight independent data that can be effectively used for natural oil slick and oil seep estimation. The designed algorithm is the first completely automated oil seep location estimator that uses SAR data. This system has been designed and implemented in the open source programming language Python allowing for a wide range of scientific applications. The ASLE segments dark objects, classifies them as slicks or L-As and estimates the slick origins. Seep locations are then estimated by spatial clustering of temporally recurrent slick origins. The ASLE can thus be used for larger data sets where the human operator will have a huge workload. The results of the designed system show that it is a promising tool for the estimation of seep locations as well as for the detection of natural oil slicks. An advantage of having a separate ASDU is that it can be used to detect natural oil slicks and oil spills in individual SAR images. The two modes of operation allow the user to set the rules for classification based on the size of the data set and the required accuracy. The novel feature-based classification used for object classification works efficiently in discriminating between slicks and L-As.

The efficiency of the ASLE and the ASDU was assessed after processing 178 SAR images of the Black Sea. The ASLE successfully estimates the locations of 9 known seeps in MODE-R when 2.5-km spatial clustering was employed. The ASDU detects the larger slicks with slick detection efficiencies of greater than 70%. The Colkheti seep and Pechori Mound, the two most dominantly seeping seeps, were detected automatically with detection efficiencies of 76% and 71%, respectively.

Since the recently launched C-band Sentinel-1 SAR satellite, launched by ESA on 03 April 2014, aims to provide free and open access data and has similar image parameters as the ENVISAT ASAR images, the ASLE will prove to be an effective tool for oil seep location estimation as well as oil slick detection in the years to come.

work would not be possible without the developers of the PYTHON libraries.

REFERENCES

[1] National Academy of Sciences (NAS), "Oilin the sea 111: Inputs, fates and effects," Washington, DC, USA, 2003.

[2] "Natural oil seeps," Woods Hole Oceanographic Institution, Woods Hole, MA, USA, 2014. [Online]. Available: http://www.whoi.edu/main/topic/natural-oil-seeps, [Accessed: 14-May-2014].

[3] O. Garcia-Pineda et al., "Using SAR images to delineate ocean oil slicks with a texture-classifying neural network algorithm (TCNNA)," Can. J. Remote Sens., vol. 35, no. 5, pp. 411–421, Oct. 2009.

[4] O. Garcia-Pineda, I. MacDonald, B. Zimmer, B. Shedd, and H. Roberts, "Remote-sensing evaluation of geophysical anomaly sites in the outer continental slope, northern Gulf of Mexico," Deep Sea Res. Part II, Topical Studies Oceanograp., vol. 57, no. 21–23, pp. 1859–1869, Nov. 2010.

[5] K. A. Kvenvolden and C. K. Cooper, "Natural seepage of crude oil into the marine environment," Geo-Marine Lett., vol. 23, no. 3/4, pp. 140–146, Dec. 2003.

[6] C. Brekke and A. H. S. S. Solberg, "Oil spill detection by satellite remote sensing," Remote Sens. Environ., vol. 95, no. 1, pp. 1–13, Mar. 2005.

[7] W. Alpers and H. A. Espedal, "Chapter 11. oils and surfactants," in Synthetic Aperture Radar Marine User's Manual, C. R. Jackson and J. R. Apel, Eds. Washington, DC, USA: U.S. Department of Commerce, National Oceanic and Atmospheric Administration, National Environmental Satellite, Data and Information Service, Office of Research and Applications, 2004, pp. 263–275.

[8] O. Garcia-Pineda, I. MacDonald, and B. Zimmer, "Synthetic aperture radar image processing using the supervised textural-neural network classification algorithm," in Proc. IEEE IGARSS, 2008, pp. IV1265–IV1268.

[9] A. H. S. Solberg, G. Storvik, R. Solberg, and E. Volden, "Automatic detection of oil spills in ERS SAR images," IEEE Trans. Geosci. Remote Sens., vol. 37, no. 4, pp. 1916–1924, Jul. 1999.

[10] T. F. N. Kanaa et al., "Detection of oil slick signatures in SAR images by fusion of hysteresis thresholding responses," in Proc. IEEE IGARSS, 2003, vol. 4, pp. 2750–2752.

[11] L. Chang, Z. S. Tang, S. H. Chang, and Y.-L. Chang, "A region-based GLRT detection of oil spills in SAR images," Pattern Recognit. Lett., vol. 29, no. 14, pp. 1915–1923, Oct. 2008.

[12] A. K. Liu, C. Y. Peng, and S. Y. Chang, "Wavelet analysis of satellite images for coastal watch," IEEE J. Ocean. Eng., vol. 22, no. 1, pp. 9–17, Jan. 1997.

[13] A. Gasull et al., "Oil spills detection in SAR images using mathematical morphology," in Proc. EUSIPCO, 2002, pp. 25–28.

[14] E. Angiuli, F. Del Frate, and L. Salvatori, "Neural networks for oil spill detection using ERS and ENVISAT imagery," in Proc. SeaSAR, Frascati, Italy, Jan. 23–26 2006, pp. 1–6.

[15] F. Del Frate, D. Latini, C. Pratola, and F. Palazzo, "PCNN for automatic segmentation and information extraction from X-band SAR imagery," Int. J. Image Data Fusion, vol. 4, no. 1, pp. 75–88, Mar. 2013.

[16] A. H. S. Solberg, C. Brekke, and P. O. Husoy, "Oil spill detection in Radarsat and Envisat SAR images," IEEE Trans. Geosci. Remote Sens., vol. 45, no. 3, pp. 746–755, Mar. 2007.

[17] B. Fiscella, A. Giancaspro, F. Nirchio, P. Pavese, and P. Trivero, "Oil spill detection using marine SAR images," Int. J. Remote Sens., vol. 21, no. 18, pp. 3561–3566, Jan. 2000.

[18] F. Del Frate, A. Petrocchi, J. Lichtenegger, and G. Calabresi, "Neural networks for oil spill detection using ERS-SAR data," IEEE Trans. Geosci. Remote Sens., vol. 38, no. 5, pp. 2282–2287, Sep. 2000.

[19] F. Pellon de Miranda et al., "Analysis of RADARSAT-1 data for offshore monitoring activities in the Cantarell Complex, Gulf of Mexico, using the unsupervised semivariogram textural classifier (USTC)," Can. J. Remote Sens., vol. 30, no. 3, pp. 424–436, Jan. 2004.

[20] M. H. Rodríguez, R. G. Cáceres, F. P. D. Miranda, and K. Bannerman, "Cantarell natural seep modelling using SAR derived ocean surface wind and meteo—oceanographic Buoy Data," in Proc. IEEE IGARSS, 2007, pp. 3257–3260.

[21] E. C. Pedroso et al., "A multi-sensor approach and ranking analysis procedure for oil seeps detection in marine environments," in Proc. IEEE IGARSS, 2007, pp. 865–870.

[22] A. M. Quintero-marmol et al., "Operational applications of RADARSAT-1 for the monitoring of natural oil seeps in the South Gulf of Mexico," in Proc. IEEE IGARSS, 2003, pp. 2744–2746.

[23] V. V. Zatyagalova and B. N. Golubov, "Application of ENVISAT SAR imagery for mapping and estimation of natural oil seeps in the south Caspian sea," in Proc. Envisat Symp., Montreux, Switzerland, Apr. 23–27, 2007, pp. 1–6.

[24] C. H. Beisl et al., "Use of genetic algorithm to identify the source point seepage slick clusters interpreted from Radarsat-1 images in the Gulf of Mexico," in Proc. IEEE IGARSS, 2004, vol. 6, no. 1, pp. 4139–4142.

[25] X. Li, C. Li, Z. Yang, and W. Pichel, "SAR imaging of ocean surface oil seep trajectories induced by near inertial oscillation," Remote Sens. Environ., vol. 130, pp. 182–187, Mar. 2013.

[26] G. Suresh, G. Heygster, G. Bohrmann, C. Melsheimer, and J.-H. Körber, "An automatic detection system for natural oil seep origin estimation in SAR images," in Proc. IEEE IGARSS, Jul. 2013, pp. 3566–3569.

[27] E. Özsoy and Ü. Ünlüata, "Oceanography of the black sea: A review of some recent results," Earth-Sci. Rev., vol. 42, no. 4, pp. 231–272, Nov. 1997.

[28] W. S. Reeburgh et al., "Black Sea methane geochemistry," Deep Sea Res. Part A, Oceanograph. Res. Papers, vol. 38, pp. S1189–S1210, Jan. 1991.

[29] A. G. Robinson, J. H. Rudat, C. J. Banks, and R. L. F. Wiles, "Petroleum geology of the Black Sea," Marine Petroleum Geol., vol. 13, no. 2, pp. 195–223, Mar. 1996.

[30] J.-H. Körber, "Remote sensing and GIS—Based analysis of hydrocarbon seeps," Ph.D. dissertation, Univ. Bremen, Bremen, Germany, 2012.

[31] "2.11.5 The Derivation of Backscattering Coefficients and RCSs in ASAR Productse," ESA Earth Online 2000–2014. [Online]. Available: https://earth.esa.int/handbooks/asar/CNTR2-11-5.htm, [Accessed: 25-Jul-2013].

[32] K. Topouzelis, V. Karathanassi, P. Pavlakis, and D. Rokos, "A new object-oriented methodology to detect oil spills using Envisat images," in Proc. Envisat Symp., 2007, pp. 1–5.

[33] J. Whitaker, "Basemap Matplotlib Toolkit 1.0.8 Documentation," 2011.

[34] F. Meyer, "Automatic screening of cytological specimens," Comput. Vis. Graph. Image Process., vol. 35, no. 3, pp. 356–369, Sep. 1986.

[35] P. Clemente-Colon and X. Yan, "Low-backscatter ocean features in synthetic aperture radar imagery," Johns Hopkins APL Tech. Dig., vol. 21, no. 1, pp. 116–121, 2000.

[36] C. Melsheimer, W. Alpers, and M. Gade, "Simultaneous observations of rain cells over the ocean by the synthetic aperture radar aboard the ERS satellites and by surface-based weather radars," J. Geophys. Res., vol. 106, no. C3, pp. 4665–4677, Mar. 2001.

[37] "QGIS Development Team Version 1.7.0 'Wroclaw', QGIS Geographic Information System. Open Source Geospatial Foundation Project," 2011.

[38] J.-H. Körber et al., "Natural oil seepage at kobuleti ridge, eastern Black Sea," Marine Petroleum Geol., vol. 50, pp. 68–82, Feb. 2014.

[39] Y. Shu, J. Li, H. Yousif, and G. Gomes, "Dark-spot detection from SAR intensity imagery with spatial density thresholding for oil-spill monitoring," Remote Sens. Environ., vol. 114, no. 9, pp. 2026–2035, Sep. 2010.

Gopika Suresh (S'13) was born in Kerala, India, in 1987. She received the M.Sc. degree in Earth Oriented Space Science and Technology (ESPACE) from the Technical University of Munich, Munich, Germany in 2011 and the B.Tech. degree in electronics and communications engineering from the University of Kerala, Kerala, India, in 2009. Since 2012, she has been working toward the Ph.D. degree at MARUM: Center for Marine Environmental Sciences and the Institute of Environmental Physics, University of Bremen, Bremen, Germany. She has previously completed her M.Sc. thesis with the Institute of Remote Sensing (IMF) at the German Aerospace Center, (DLR), Oberpfaffenhofen, Munich.

Her research involves the automatic detection, mapping, and quantification of offshore oil seepage using synthetic aperture radar (SAR) images. Her research interests are in the field of image processing with applications to spaceborne SAR data, and she is an expert in algorithm development for ocean remote sensing applications, SAR interferometry, differential interferometry, and geoinformation systems-related applications.

Christian Melsheimer was born in Kamen, Germany, in 1967. He received the Diploma degree M.Sc. in physics from the University of Dortmund, Dortmund, Germany, in 1994 and the Ph.D. degree from the University of Hamburg, Hamburg, Germany, in 1998.

From 1995 to 1998, he was with the Satellite Oceanography Group, Institute of Oceanography, University of Hamburg, Hamburg, Germany, where his work concentrated on radar imaging of the ocean surface and on remote sensing of rain over the ocean. From 1999 to 2002, he was with the Centre for Remote Imaging, Sensing, and Processing (CRISP), National University of Singapore, Singapore, where he studied various oceanic phenomena as visible on satellite radar images and satellite images taken in visible/near-infrared light. Since 2002, he has been with the Institute of Environmental Physics (IUP), University of Bremen, Bremen, Germany, where he does research in microwave remote sensing of atmosphere, sea and land, with special emphasis on the polar regions.

Jan-Hendrik Körber received the Diploma degree in physical geography, geosciences, and biology and the Ph.D. degree in marine geology from the University of Bremen, Bremen, Germany, in 2009 and 2012 respectively. During his undergraduate studies, he specialized in geoinformatics, remote sensing, and spatial and ecosystem modeling. During his graduate studies and the Ph.D. degree, he conducted research on remote sensing and geoinformation systems (GIS)-based analyses of hydrocarbon seeps and related geological processes.

He is currently with MARUM: Center for Marine Environmental Sciences. He is an expert in GIS, spatial data fusion and analyses and hydroacoustic seafloor and water column imaging. Currently, he is working on the development of a novel autonomous underwater vehicle for the detection and sampling of hydrocarbon seeps.

Gerhard Bohrmann was educated in the field of marine geology and received the Ph.D. degree in geosciences from the Christian-Albrechts-University in Kiel, Kiel, Germany, in 1988.

He worked as a Postdoctoral Fellow for three years with the Alfred-Wegener-Institute for Polar and Marine Science, Bremerhaven, Germany, before he became an Assistant Professor in marine geology with GEOMAR, Kiel. Since 2002, he has been a Professor of general geology and marine geology with the Department of Geosciences, Bremen University, Bremen, Germany, and since 2005, he additionally has been Vice Director of the DFG Research Center/Excellence Cluster "The Ocean in the Earth System" MARUM, Bremen. During the last 20 years, he was involved in numerous seep-related investigations at active plate boundaries such as the Aleutian subduction zone, Cascadia Margin, Scotia Sea, Taiwan, China, Japan, and along the Middle American trench. In the Black Sea, Mediterranean, in Congo, and Niger deep sea fans, he studied near-seafloor gas hydrate outcrops and performed interdisciplinary studies at seep sites. He participated in more than 40 research cruises, in which he often coordinated the research and took the position of a Chief Scientist.